



Crystal Plasticity-Based Spalling Damage Model for Ductile Metals

Chen Li^{1,2} · Hai-Ying Wang^{1,2} · Lan-Hong Dai^{1,2}

Received: 23 March 2022 / Revised: 11 August 2022 / Accepted: 15 August 2022 / Published online: 19 October 2022
© The Chinese Society of Theoretical and Applied Mechanics 2022

Abstract

Spalling is a typical tensile failure that results from the coupling evolution of microstructure and microdamage under high strain-rate loading. To understand the spalling damage behavior of polycrystalline materials at mesoscale, this paper develops a spalling model by integrating the crystal plasticity theory and the microvoid growth theory. The model is implemented in ABAQUS simulation via the VUMAT subroutine to simulate a planar impact process of copper, and the results are compared with experimental data. Due to the inhomogeneity of crystal plastic slip, the local stress fluctuates severely near the grain boundary. Therefore, without introducing the fluctuation in the threshold stress for microdamage evolution, this model can simulate the heterogeneous feature of microvoid nucleation, growth, and coalescence in materials. The results show that microvoids tend to nucleate at 25°–50° misorientation angle grain boundaries, which undergo a high probability of stress fluctuation.

Keywords Spalling · Crystal plasticity · Microvoid nucleation and growth · Grain boundary · Finite element method

1 Introduction

Spalling is a typical tensile failure that results from the nucleation, growth, and coalescence of microvoids or microcracks produced in materials under high strain-rate loading [1–3]. In the spalling process, the microstructural features of materials, e.g., the grain size, grain orientation, precipitates, inclusions, etc., evolve under impact loading and cause the evolution of microdamage. The coupling between the microstructural and microdamage evolution and the external impact loading poses fundamental challenges to spalling prediction.

Numerous efforts have been devoted to modeling the microstructural and microdamage evolution in the spalling process [4–9]. The dynamic crystal plasticity theory is one of the fundamental theories for describing plastic deformation [10–18], which is widely used in simulations of material impact dynamic process, microstructural evolution, and dynamic failure. For example, Chao Ling [19] used

a reduced micromorphic single crystal plasticity model to simulate void growth in ductile metals; Clayton [20, 21] simulated a spalling process with only grain boundary damage based on the weak connection model; Wilkerson and Ramesh [22, 23] developed the micro- and nano-scale void growth theory based on the dislocation density theory and the relativistic effect of dislocations. Although these studies help understand the dynamic deformation behavior and failure process of materials, a predicting model involving both intragranular and grain boundary microdamage evolution is still lacking.

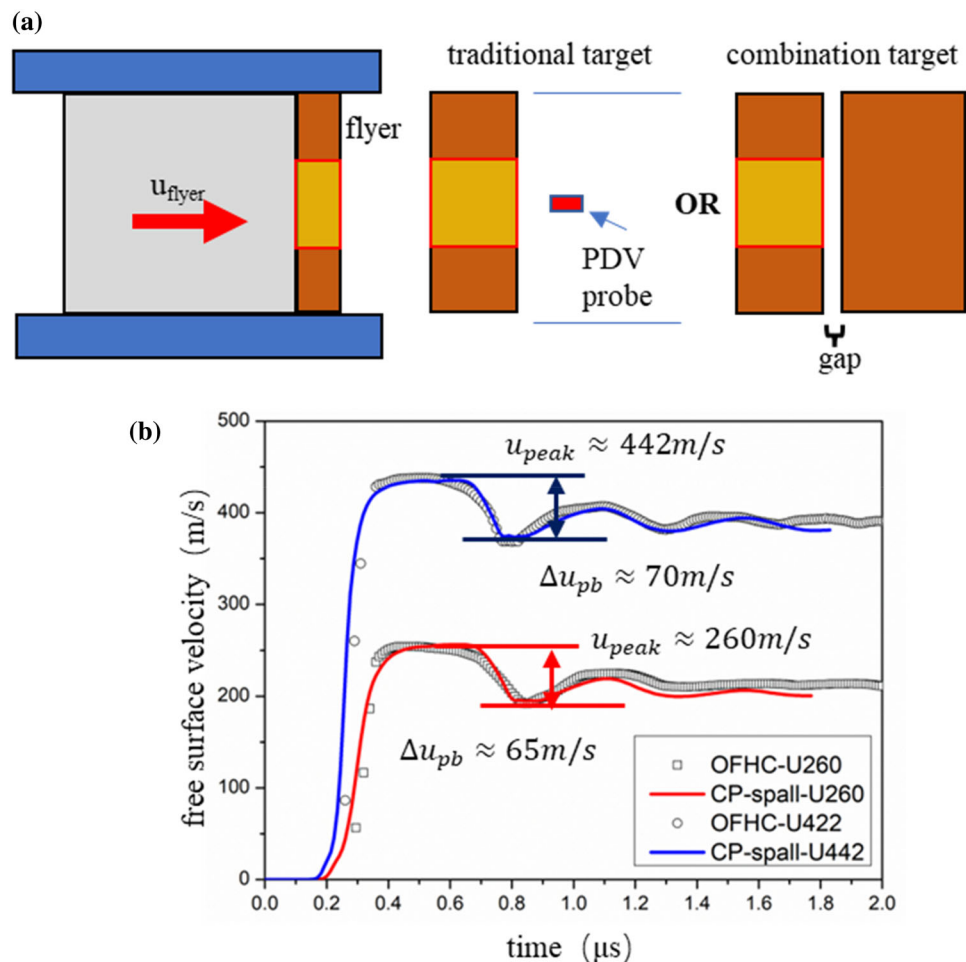
To investigate the effect of grain boundaries on spalling, in this study, we first performed plate impact experiments of high-purity polycrystalline oxygen-free high-thermal-conductivity (OFHC) copper samples on a one-stage light-gas gun; and then developed a new spalling damage model based on crystal plasticity and microvoid nucleation and growth theory. The model was implemented in the finite element simulation via the VUMAT subroutine of ABAQUS to investigate how damage nucleates and propagates in the target. The agreement between the simulation and experiments proves the validation of the new model. The simulation shows that resulting from high-stress fluctuations on grain boundaries with 25°–50° misorientation angle, microvoids are prone to nucleate on these boundaries in the initial damage evolution stage. With the increase in loading time,

✉ Hai-Ying Wang
why@lnm.imech.ac.cn

¹ State Key Laboratory of Nonlinear Mechanics, Institute of Mechanics, Chinese Academy of Sciences, Beijing 100190, China

² School of Engineering Science, University of Chinese Academy of Sciences, Beijing 100049, China

Fig. 1 **a** Experimental setup, the traditional target for recording particle velocity curve by PDV probe, the combination target for freezing damage; **b** the particle velocity profiles of the free surface of the targets, where the discrete points are experimental data, and the curves are obtained from the finite element simulation



intragranular microvoids dominate damage evolution, followed by the coalescence of microvoids inducing final spalling.

2 Plate Impact Experiment

The plate impact experiments of oxygen-free high-thermal-conductivity (OFHC) copper were conducted on a one-stage light-gas gun, as shown in Fig. 1a. The study involved three experiments, denoted as OFHC-U260, OFHC-U442, and OFHC-U442F. OFHC-U260 and OFHC-U442 adopted the traditional target and recorded the free-surface velocity profiles by a photonic Doppler velocimeter (PDV), as shown in Fig. 1b. OFHC-U442F adopted the combination target to achieve damage freezing [24] (due to the back target, the free-surface curve could not be recorded, we used the same pressure-to-mass ratio to drive the flyer to obtain a speed similar to that of OFHC-U442), and the equation for tensile pulse width is:

$$\tau \approx \frac{d_{\text{gap}}}{u_p} \quad (1)$$

Table 1 The details of three shot experiments

	OFHC-U260	OFHC-U442	OFHC-U442F
The diameter of targets	30 mm		
The diameter of flyers	> 30 mm		
The thickness of targets	2.24 mm	2.20 mm	2.20 mm
The thickness of flyers	1.20 mm	1.24 mm	1.24 mm
Peak stress	4.66 GPa	8.29 GPa	—
Spall strength	1.13 GPa	1.22 GPa	—

where d_{gap} is the gap between combination targets, u_p is the free-surface particle velocity, and τ is tensile pulse width. For OFHC-U442F, $d_{\text{gap}} = 40 \mu\text{m}$, $u_p \approx 442 \text{ m/s}$, so $\tau \approx 90 \text{ ns}$. The details of the three experiments are shown in Table 1.

The electron backscatter diffraction (EBSD) microscope images clearly show that the sample has a grain size of about $300\text{ }\mu\text{m}$ (Fig. 2a).

The peak stress σ_{peak} can be approximately calculated as:

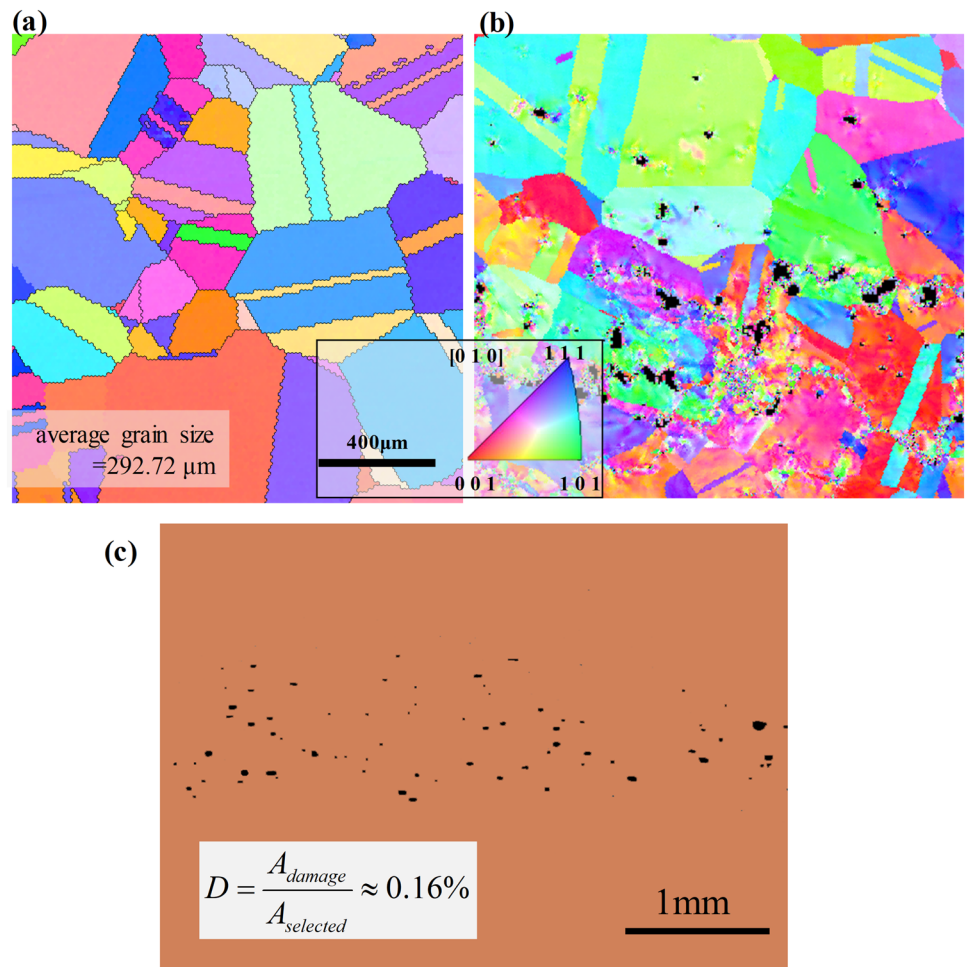
$$\sigma_{\text{peak}} \approx \frac{\rho_0}{2} \left(c_0 + \frac{1}{2} s u_{\text{peak}} \right) u_{\text{peak}} \quad (2)$$

where ρ_0 is the initial density of OFHC, c_0 is the sound velocity in the material at zero pressure, s is the linear Hugoniot slope coefficient, and u_{peak} is the peak velocity of free-surface particles. The spall strength is calculated from the pullback velocity with the sound velocity approximation:

$$\sigma_{\text{spall}} \approx \frac{\rho_0}{2} c_0 \Delta u_{\text{pb}} \quad (3)$$

where Δu_{pb} is the pullback velocity, which is the difference between peak and rebound velocities. According to the above formulae, the corresponding calculation results are shown in Table 1.

Fig. 2 **a** IPF map of initial oxygen-free high-thermal-conductivity (OFHC) copper sample; **b** IPF maps of samples of OFHC-U442F; **c** damage statistics of OFHC-U442F (the black spots are microvoids)



After the impact test, the targets of OFHC-U442F were cut, ground, and polished for EBSD observation. As shown in Fig. 2b, the microvoids spread across the grain boundaries, near-grain boundaries and inside grains. Figure 2c is an optical microscope photo, which is used for damage statistics.

3 Theoretical Model

In this section, a new theoretical model is developed, which integrates shock dynamics of solid, the rate-dependent crystal plasticity theory [25], and the nucleation and growth theory of microvoids [26].

3.1 Volumetric Stress

The update of the volumetric stress in the model is through the shock dynamics of solid. Based on the $u_s - u_p$ equation of state of solid impact and the Rankine–Hugoniot relationship [27] (mass, momentum, and energy continuity conditions of

impact), the relationship between volume change and volumetric stress under impact loading is:

$$\Delta\sigma^V = -\Delta p = \frac{\rho_0^2 c_0^2 \Delta V}{(1 + s\rho_0 \Delta V)^2} \quad (4)$$

where u_s is the velocity of shock wave, u_p is the velocity of particle, p is pressure, σ^V is volumetric stress, which equals negative pressure, $V=1/\rho$ is specific volume, and ρ is the current density of the material.

According to the Mie–Grüneisen equation of state, considering the contribution of plastic work to volumetric stress, Eq. (4) is modified as:

$$\Delta\sigma^V = \frac{\rho_0^2 c_0^2 \Delta V}{(1 + s\rho_0 \Delta V)^2} - \frac{\gamma}{V} 0.9W^P \quad (5)$$

where γ is the Grüneisen coefficient, and the second term on the right-hand side represents the contribution of the plastic work by assuming the work-heat conversion coefficient to be 0.9. The plastic work can be calculated from the following equation:

$$dW^P = \sigma' d\epsilon' + \sigma^V df \quad (6)$$

where f is the porosity of the damage element. In Eq. (6), the plastic work consists of two parts: one is the contribution of the work of deviatoric stress σ' on the deviatoric strain ϵ' , the other is the contribution of volumetric stress σ^V on void expansion df .

3.2 Deviatoric Stress

The update of deviatoric stress in the model is made through the crystal plasticity theory [25]. The total deformation gradient tensor \mathbf{F} can be decomposed as:

$$\mathbf{F} = \mathbf{F}^* \cdot \mathbf{F}^P \quad (7)$$

where superscript $*$ denotes lattice deformation, and superscript P denotes crystal slip. The deformation rate is given by:

$$\mathbf{D} = \text{sym}[\dot{\mathbf{F}} \cdot (\mathbf{F})^{-1}] = \mathbf{D}^* + \mathbf{D}^P \quad (8)$$

where $\text{sym}[\cdot]$ means the symmetric part of the tensor, and \mathbf{D} can be divided into elastic part \mathbf{D}^* and plastic part \mathbf{D}^P . The elastic deformation rate can be further decomposed into spherical and deviatoric parts as:

$$\mathbf{D}^* = D_m \mathbf{I} + \mathbf{D}' \quad (9)$$

where D_m is the value of spherical strain rate, \mathbf{I} is the identical second-order tensor, and \mathbf{D}' is the deviatoric part of elastic deformation rate tensor.

Since plastic deformation does not generate stress, the Cauchy stress is expressed as:

$$\overset{\nabla}{\sigma} + \sigma(\mathbf{I}:\mathbf{D}^*) = \mathbb{L}:\mathbf{D}^* \quad (10)$$

where $\overset{\nabla}{\sigma}$ is the Jaumann rate of Cauchy stress σ , and \mathbb{L} is the elastic modulus tensor, which has three independent crystallographic stiffnesses of materials, C_{11} , C_{12} , and C_{44} .

The rate of plastic deformation gradient tensor \mathbf{F}^P is related to the slipping rate $\dot{\gamma}^{(\alpha)}$ of the slip system α :

$$\dot{\mathbf{F}}^P \cdot (\mathbf{F}^P)^{-1} = \sum_{\alpha} \dot{\gamma}^{(\alpha)} \mathbf{s}^{(\alpha)} \mathbf{m}^{(\alpha)} \quad (11)$$

where the sum ranges over all activated slip systems, $\mathbf{s}^{(\alpha)}$ and $\mathbf{m}^{(\alpha)}$ are the unit vectors of the slip direction and the normal to the slip plane, respectively.

The corresponding resolved shear stress $\tau^{(\alpha)}$ of the slip system α is:

$$\tau^{(\alpha)} = \mathbf{m}^{(\alpha)} \cdot \frac{\rho_0}{\rho} \sigma \cdot \mathbf{s}^{(\alpha)} \quad (12)$$

Based on the Schmid law, the slipping rate $\dot{\gamma}^{(\alpha)}$ of the slip system α in a rate-dependent crystalline solid is determined by $\tau^{(\alpha)}$ as:

$$\dot{\gamma}^{(\alpha)} = \dot{\gamma}^{(\alpha)} \hat{f}^{(\alpha)} \left(\frac{\tau^{(\alpha)}}{g^{(\alpha)}} \right) \quad (13)$$

where $\dot{\gamma}^{(\alpha)}$ and $g^{(\alpha)}$ are the reference strain rate and the current strength of the slip system α , respectively, and $\hat{f}^{(\alpha)}$ is non-dimensional functions describing the dependence of strain rate on stress. In the current study, we follow the simple law proposed by Hutchinson [28] as:

$$\hat{f}(x) = x|x|^{N-1} \quad (14)$$

The strain hardening is characterized through the incremental relation as:

$$g^{(\alpha)} = \sum_{\beta} h_{\alpha\beta} \dot{\gamma}^{(\beta)} \quad (15)$$

where the sum ranges over all activated slip systems, and $h_{\alpha\beta}$ is the slip hardening moduli of slip. $h_{\alpha\alpha}$ (no sum) and $h_{\alpha\beta}$ ($\alpha \neq \beta$) are self and latent hardening moduli, respectively. We use the expression of Bassani and Wu [29] for the hardening moduli to describe the three-stage hardening of

crystalline materials. Their expression depends on the shear strains $\underline{\gamma}^{(\alpha)}$ of all slip systems as:

$$h_{\alpha\alpha} = \left\{ (h_0 - h_s) \operatorname{sech}^2 \left| \frac{(h_0 - h_s) \underline{\gamma}_0}{\tau_s - \tau_0} \right| + h_s \right\} \hat{G}(\gamma^{(\beta)}; \beta \neq \alpha) \quad \text{no sum on } \alpha \quad (16)$$

$$h_{\beta\alpha} = q h_{\alpha\alpha} \quad (\beta \neq \alpha) \quad (17)$$

where h_0 is the initial hardening modulus, h_s is the hardening modulus for easy slip stage, τ_0 is the yield stress, τ_s is the break-through stress, and \hat{G} is the cross-slip-related function given by:

$$\hat{G}(\gamma^{(\beta)}; \beta \neq \alpha) = 1 + \sum_{\beta \neq \alpha} \tilde{f}_{\alpha\beta} \tanh \left(\frac{\gamma^{(\beta)}}{\gamma_0} \right) \quad (18)$$

where $\underline{\gamma}_0$ is the amount of slip of the peak strength, and $\tilde{f}_{\alpha\beta}$ represents the interaction coefficient of the slips.

3.3 Void Nucleation and Growth Law

The critical volumetric stress σ_{nu}^V determines the spalling damage nucleation. When the volumetric stress of the element is greater than σ_{nu}^V , microvoid nucleates. σ_{nu}^V is assumed to be equal everywhere in the simulation. No initial pressure fluctuations are set, and no interface is set as a weak point.

Once the microvoid nucleates, the growth of the microvoid in the element will be considered. For an element with radius b containing a microvoid with radius a , the porosity of the element is given by:

$$f = \frac{a^3}{b^3} \quad (19)$$

According to the analysis of Czarnota et al. [30], the evolution of the microvoid radius a is governed by the following differential equation:

$$\sigma^V - \sigma_{\text{gr}}^V = \rho \left\{ a \ddot{a} \left(1 - f^{1/3} \right) + \frac{3}{2} \dot{a}^2 \left(1 - \frac{4}{3} f^{1/3} + \frac{1}{3} f^{4/3} \right) \right\} \quad (20)$$

where σ_{gr}^V is the threshold stress for microvoid growth, which equals to the smaller one of σ_{nu}^V and the growth stress in the Gurson model σ_G^V :

$$\sigma_{\text{gr}}^V = \min(\sigma_{\text{nu}}^V, \sigma_G^V) \quad (21)$$

The growth pressure in the Gurson model is:

$$\sigma_G^V = \frac{2k^{\text{poly}}}{3q_2} \ln \left(\frac{1}{q_1 f} \right) \left\{ \varepsilon_0^{\text{poly}} + \varepsilon^{\text{pre}} + \frac{2}{3q_2} \ln \left[\frac{(q_1 f)^{-f/(1-f)}}{(1-f)} \right] \right\}^n$$

$$\times \left\{ \dot{\varepsilon}_0^{\text{poly}} + \frac{2}{3q_2} \ln \left(\frac{1}{q_1 f} \right) \frac{\dot{f}}{(1-f)^2} \right\}^m \quad (22)$$

where the constant coefficients $q_1 = q_2 = 1$, ε^{pre} is cumulative plastic equivalent strain, m and n are the strain-rate sensitivity exponent and strain hardening exponent, respectively, $\dot{\varepsilon}_0^{\text{poly}}$ and $\varepsilon_0^{\text{poly}}$ are the reference strain rate and the reference strain, respectively, and k^{poly} is a scaling factor for the flow stress level.

3.4 Reduction in Stiffness and Strength Caused by Temperature Increase and Damage Evolution

The stiffness of the material is reduced due to temperature rise and damage evolution. The initial equivalent shear modulus is [31]:

$$G_0 = \frac{C_{11} - C_{12} + 3C_{44}}{5} \quad (23)$$

The initial bulk modulus K_0 is calculated by derivation of Eq. (4):

$$K_0 = -V \frac{d\Delta p}{d\Delta V} = V \frac{\rho_0^2 c_0^2 (1 - s\rho_0 \Delta V)}{(1 + s\rho_0 \Delta V)^3} \quad (24)$$

The temperature increment can be calculated as [27]:

$$\Delta T = \frac{\Delta E + p \Delta V}{c_v} - T \frac{\gamma}{V} \Delta V \quad (25)$$

where c_v is the specific heat. Temperature rise ΔT can be obtained from the simultaneous Eqs. (5), (6), and (25).

The element stiffness is reduced with microdamages and temperature [32] as:

$$C_{ij} = C_{ij0} (1 - f) \left(1 - \frac{6K_0 + 12G_0}{9K_0 + 8G_0} f \right) \frac{T_r - T}{T_r} \quad (26)$$

$$K = K_0 \frac{4G_0(1-f)}{3K_0 f + 4G_0} \frac{T_r - T}{T_r}$$

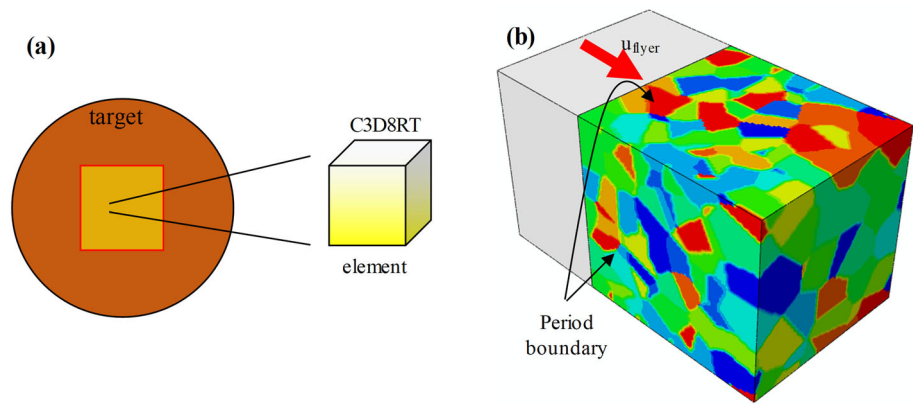
where T_r is the reference temperature equal to the melting temperature minus the loading temperature.

When the element contains damage, the equivalent strength and the effective cutting stress of the slip system are reduced as:

$$\hat{g}^{(\alpha)} = g^{(\alpha)} \cdot (1 - f), \quad \hat{\tau}^{(\alpha)} = \tau^{(\alpha)} / (1 - f) \quad (27)$$

The purpose of this model is to discuss the influence of inhomogeneity of plastic slip on the evolution of spalling damage. This model contains some approximate assumptions, for example, the variation of slip strength with temperature is not considered, and the quasi-static bearing capacity

Fig. 3 **a** Selection of the central region (yellow part) for finite element analysis; **b** finite element polycrystalline models, where the selected area of the target is dyed by the Euler angle ϕ , the white area is the flyer, and the flyer and target adopt periodic boundary conditions perpendicular to the impact direction



of material with voids is calculated by the Gurson model. When the impact velocity is not high (the temperature rise is not high) and the details of the edge of each void are not considered, this model can give reliable averaged calculation results.

4 Finite Element Simulation

Commercial finite element software ABAQUS/Explicit is utilized to simulate the planar impact test of OFHC. The target plate is $2\text{ mm} \times 2\text{ mm} \times \text{thickness of the sample}$ (Fig. 3a), with periodic boundaries perpendicular to the impact direction. The finite element polycrystalline model is generated by Voronoi polyhedrons of 300 random seeds, and three Euler angles determine the crystallographic orientation. The Euler angles are also randomly generated in the model. Figure 3b shows the polycrystalline models established for calculation. The C3D8RT element (an 8-node thermally coupled brick, trilinear displacement and temperature, reduced integration) is used in the simulation. A VUMAT subroutine is written to implement the above constitutive model in Sect. 3 in the FEM simulation. The corresponding parameters are shown in Table 2. The finite element simulation of OFHC-U260 and OFHC-U442 are carried out, which are denoted as CP-spall-U260 and CP-spall-U442, respectively.

In the simulation, to reduce the computational complexity, an equivalent polycrystalline plastic model is employed for the flyer material. The deviatoric viscoplastic flow follows the form of Czarnota et al. [27] A power-law equation is adopted to characterize the flow stress σ_y^{poly} , taking both strain hardening and strain-rate sensitivity into account:

$$\sigma_y^{\text{poly}} = k^{\text{poly}} \left(\dot{\varepsilon}_0^{\text{poly}} + \dot{\varepsilon}_{\text{eq}}^{\text{poly}} \right)^m \left(\varepsilon_0^{\text{poly}} + \varepsilon_{\text{eq}}^{\text{poly}} \right)^n \quad (28)$$

In Eq. (28), the corresponding symbols have the same meaning as Eq. (22).

5 Results and Discussions

5.1 Model Validation

To validate the constitutive model, we compare the simulation results of CP-spall-U442 with the experimental results of OFHC-U442F, and find that the experimentally measured damage in Fig. 6b (the red spot) falls near the simulated damage evolution curve (the tensile region appears at $\sim 800\text{ ns}$ in CP-spall-U442, so the damage state of OFHC-U442F is the state of $\sim 890\text{ ns}$), which proves the validity of the constitutive model.

5.2 Stress Wave Propagation and Damage Evolution

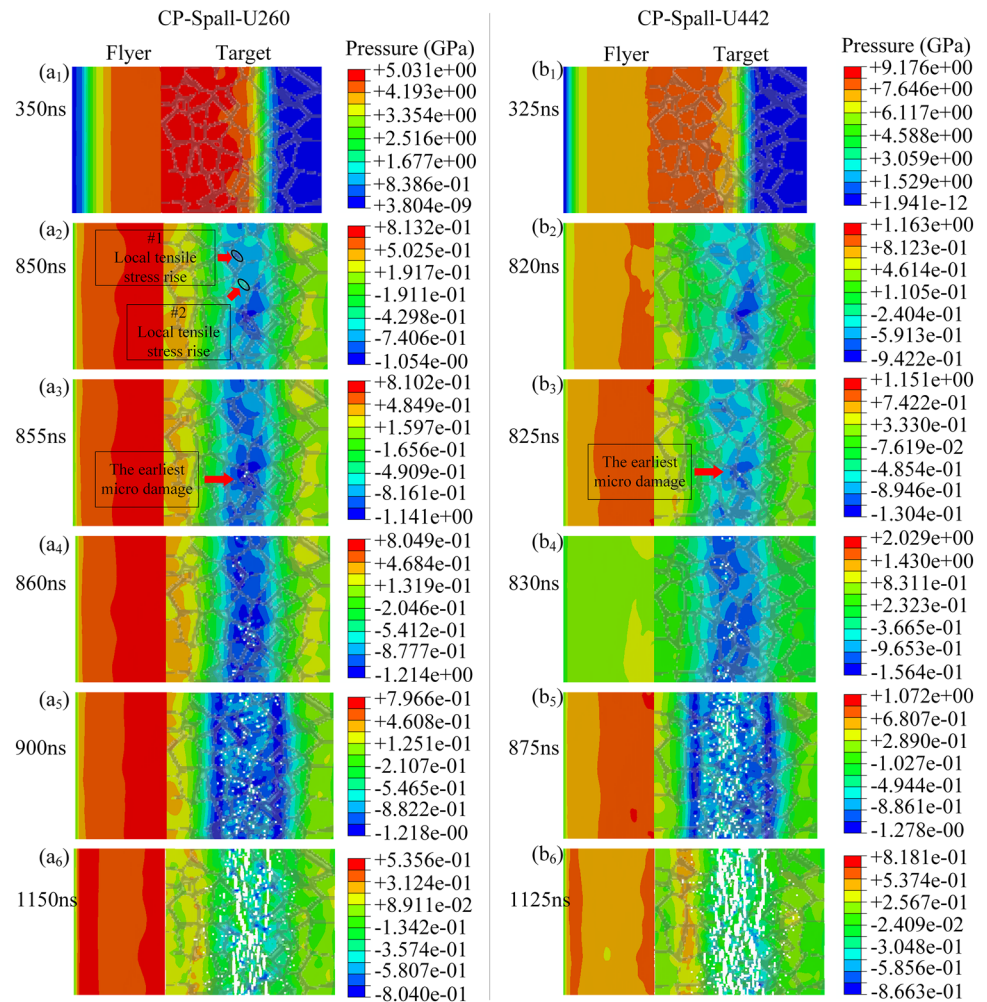
Figure 4 shows the stress wave propagation and the induced damage evolution in the simulated sample. In the shock compression stage, the wave head of the elastic precursor wave (the blue–green interface) is relatively flat, but the subsequent plastic wave head (the red–yellow interface) has noticeable stress fluctuations (Fig. 4a₁b₁). The shock waves are reflected on the free surfaces to form rarefaction waves, which transmit into the material and generate tensile stress inside the material. Since the plastic deformation of the crystal is not uniform, the tensile pressure fluctuates on grain boundaries (Fig. 4a₂b₂). When the tensile pressure is greater than the critical value $\sigma_{\text{nu}}^{\text{V}}$, microvoids nucleate on the grain boundaries (Fig. 4a₃b₃). With time going by, more microvoids nucleate on or near the grain boundaries (Fig. 4a₄b₄). However, many intragranular microvoids appear and disperse in the spall region (Fig. 4a₅b₅). In the later stage of damage evolution, the microvoids grow and coalesce, and the sample basically loses the load-bearing capacity (Fig. 4a₆b₆).

5.3 Grain Boundaries and Initial Nucleation Sites

We define an element as a grain boundary element (GBE) when the eight nodes of the element are not all in the same Voronoi polyhedron, as a near-grain-boundary element

Table 2 Parameters in the simulation

Name	Symbol	Numerical value	Remark
Density	ρ_0	8.93 g/cm ³	From [31]
Elastic parameters	C_{11}, C_{12}, C_{44}	176, 118, 61 GPa	
Sound velocity	c_0	3.9 km/s	From [27]
Linear Hugoniot slope coefficient	s	1.49	
Grüneisen parameter	γ_0	2.0	
Specific heat	c_v	384.9×10^{-6} kJ/(g·°C)	
Crystal plasticity coefficient	$N, \dot{a}_0, h_0, h_s, \tau_0, \tau_s, f_{\alpha\beta}, q_{\alpha\beta}$	2.0, 0.05 s ⁻¹ , 1.5 GPa, 0.5 GPa, 0.1 GPa, 0.3 GPa, 0.03, 0.01	Determination of parameters by curve fitting (Fig. 1b)
The critical nucleation volumetric stress	σ_{nu}^V	1.11 GPa	
Critical damage	f_c	0.024	
Equivalent polycrystalline coefficient	$k^{poly}, \varepsilon_0^{poly}, m, \varepsilon_0^{poly}, n$	0.3 GPa·s ^m , 100 s ⁻¹ , 0.48, 0.02, 0.4	Determination of the parameters by tensile simulation of the crystal plasticity model
The size of elements	b_0	25 μ m	

Fig. 4 Pressure and damage evolution in target plates, where the shadow parts on the targets are the grain boundaries, and the white points are the damage (deleted unit)

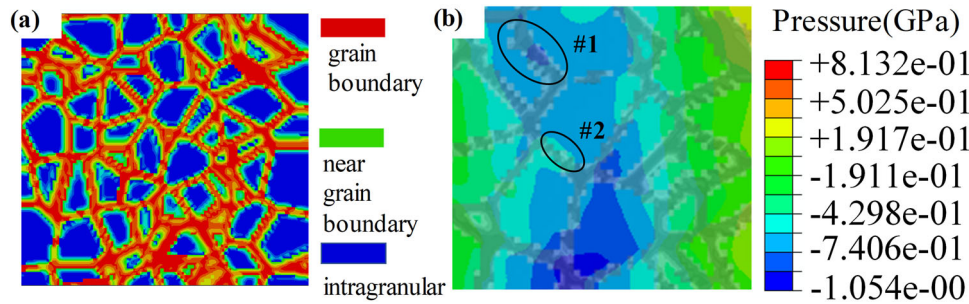


Fig. 5 **a** A slice diagram of the polycrystalline target, where the red regions represent the grain boundary elements (GBE), the green regions represent the near grain boundary elements (NGBE), and the blue

regions represent the intragranular elements (IGE); **b** inhomogeneous distribution of pressure near grain boundaries before microdamage nucleation (CP-spall-U442 820 ns)

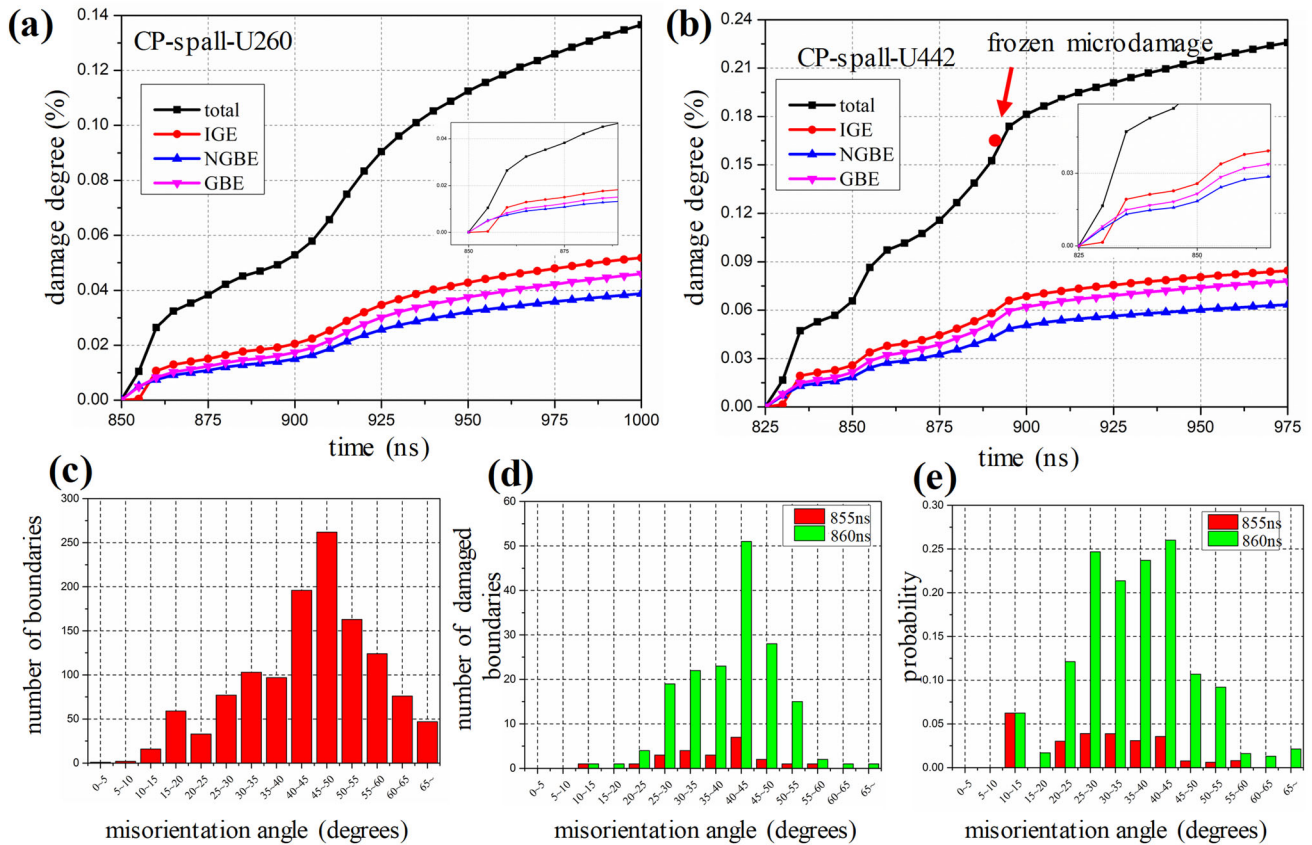


Fig. 6 **a** and **b** Damage evolution in different types of elements (the red point in **(b)** is damage statistics results of OFHC_U442F); **c** statistics of misorientation angles of grain boundaries in the spalling damage zone

(shot CP-spall-U260); **d** and **e** statistics and the probability of misorientation angles of grain boundaries with damage at 855 ns and 860 ns (shot CP-spall-U260)

(NGBE) whenever there is a grain boundary element around it, and the others as intragranular elements (IGE) (Fig. 5a). In the simulations, the "random" nucleation of microdamage is due to the inhomogeneity of the stress distribution caused by crystal slippage, as shown (Fig. 5b), the volumetric stress of #1 grain boundary is greater than the average value near the spall area, so it is more prone to nucleation damage, while #2 grain boundary, on the contrary, prevents damage nucleation.

The microvoids in different types of elements are counted and analyzed. Figure 6a and b shows the evolution of damage in these elements with time. The damage degree D is equal to the number of deleted elements N_{deleted} multiplied by the critical damage degree f_c and divided by the number of total elements N_{total} :

$$D = \frac{N_{\text{deleted}} f_c}{N_{\text{total}}} \quad (29)$$

As shown in the insets in Fig. 6a and b, the initial damage evolution is dominated by damage in grain boundary elements and near-grain-boundary elements. After that, the damage evolution in grain boundary elements and near-grain-boundary elements slow down. Meanwhile, the damage in intragranular elements notably increases, manifested by relatively isolated and dispersed microvoids in grains, as shown in Fig. 4a₅ and b₅. Then, the coalescence of microvoids dominates the damage evolution until an interconnected network of microvoids forms, as shown in Fig. 4a₆ and b₆.

To understand the impact of grain boundary type on initial nucleation of microvoid, we analyze the misorientation angle distribution in the spalling damage zone. Figure 6c–e plots the distributions of the number of grain boundaries with different misorientation angles in the intact sample, the number of damaged grain boundaries with different misorientation angles, and the corresponding probability of the damaged grain boundary, respectively. It can be seen that the grain boundary with 25°–50° is more prone to damage, which is consistent with the relevant experimental observations [9]. Hence, it can be inferred that the grain boundaries with misorientation angles of 25°–50° are more susceptible to damage even without a weak interface, which may result from the heterogeneous stress distribution in the spalling region.

6 Summary

In this paper, a new spalling model, which combines the crystal plasticity and dynamic microvoid growth models, has been developed and implemented via the VUMAT subroutine in ABAQUS. The numerical results are compared with those of plate impact experiments of OFHC. The agreement between the simulation and experiments proves the validation of the new model. The simulation shows that microvoids are prone to nucleate on grain boundaries or near-grain boundaries at first, while with the increase in loading time, intragranular microvoids dominate damage evolution. In addition, grain boundaries with 25°–50° misorientation angle are more susceptible to damage due to higher stress.

Acknowledgments This work was supported by the NSFC (Nos.12172367, 11790292, 11988102, and U2141204), the Strategic Priority Research Program (Nos. XDB22040302 and XDB22040303).

Declarations

Conflict of interest The authors declared that they have no conflicts of interest in this work. And we declare that we do not have any commercial or associative interest representing a conflict of interest in connection with the work submitted.

References

1. Bai Y, Wang H, Xie M, Ke F. Statistical mesomechanics of solid, linking coupled multiple space and time scales. *Adv Mech*. 2006;36(2):286–305.
2. Meyers MA, Aimone CT. Dynamic fracture by spalling of metals. *J Met*. 1982;35(12):A55–A55.
3. Curran DR, Seaman L, Shockey DA. Dynamic failure of solids. *Phys Rep*. 1987;147(5):253–388. [https://doi.org/10.1016/0370-1573\(87\)90049-4](https://doi.org/10.1016/0370-1573(87)90049-4).
4. Escobedo JP, Cerreta EK, Dennis-Koller D, Patterson BM, Bronkhorst CA. Influence of shock loading kinetics on the spall response of copper. In: Buttler W, Furlanetto M, Evans W, editors. 18th Aps-Scm and 24th Airapt, Pts. Berlin: Springer; 2014. p. 1–19.
5. Remington TP, Hahn EN, Zhao S, Flanagan R, Mertens JCE, Sabbaghianrad S, Langdon TG, Wehrenberg CE, Maddox BR, Swift DC, Remington BA, Chawla N, Meyers MA. Spall strength dependence on grain size and strain rate in tantalum. *Acta Mater*. 2018;158:313–29. <https://doi.org/10.1016/j.actamat.2018.07.048>.
6. Cheng M, Li C, Tang MX, Lu L, Li Z, Luo SN. Intragranular void formation in shock-spalled tantalum: mechanisms and governing factors. *Acta Mater*. 2018;148:38–48. <https://doi.org/10.1016/j.actamat.2018.01.029>.
7. Cerreta EK, Escobedo JP, Perez-Bergquist A, Koller DD, Trujillo CP, Gray III GT, Brandl C, Germann TC. Early stage dynamic damage and the role of grain boundary type. *Scr Mater*. 2012;66(9):638–41. <https://doi.org/10.1016/j.scriptamat.2012.01.051>.
8. Perez-Bergquist AG, Cerreta EK, Trujillo CP, Cao F, Gray GT. Orientation dependence of void formation and substructure deformation in a spalled copper bicrystal. *Scr Mater*. 2011;65(12):1069–72. <https://doi.org/10.1016/j.scriptamat.2011.09.015>.
9. Wayne L, Krishnan K, DiGiacomo S, Kovvali N, Peralta P, Luo SN, Greenfield S, Byler D, Paisley D, McClellan KJ, Koskelo A, Dickerson R. Statistics of weak grain boundaries for spall damage in polycrystalline copper. *Scr Mater*. 2010;63(11):1065–8. <https://doi.org/10.1016/j.scriptamat.2010.08.003>.
10. Nie J, Liu Y, Lin P, Xie Q, Liu Z. A crystal plasticity model with irradiation effect for the mechanical behavior of FCC metals. *Acta Mech Solida Sin*. 2019;32(6):675–87. <https://doi.org/10.1007/s10338-019-00145-z>.
11. Xie Q, Zhu Z, Kang G. Crystal-plasticity-based dynamic constitutive model of AZ31B magnesium alloy at elevated temperature and with explicit plastic-strain-rate control. *Acta Mech Solida Sin*. 2020;33(1):31–50. <https://doi.org/10.1007/s10338-019-00130-6>.
12. Hill R. Generalized constitutive relations for incremental deformation of metal crystals by multislip. *J Mech Phys Solids*. 1966;14(2):95–102. [https://doi.org/10.1016/0022-5096\(66\)90040-8](https://doi.org/10.1016/0022-5096(66)90040-8).
13. Asaro RJ. Micromechanics of crystals and polycrystals. In: Hutchinson JW, Wu TY, editors. *Advances in applied mechanics*. Amsterdam: Elsevier; 1983. p. 1–115.
14. Hill R. The essential structure of constitutive laws for metal composites and polycrystals. *J Mech Phys Solids*. 1967;15(2):79–95. [https://doi.org/10.1016/0022-5096\(67\)90018-X](https://doi.org/10.1016/0022-5096(67)90018-X).
15. Asaro RJ. Crystal plasticity. *J Appl Mech*. 1983;50(4b):921–34. <https://doi.org/10.1115/1.3167205>.
16. Yuan S, Zhu Y, Huang M, Liang S, Li Z. Dislocation-density based crystal plasticity model with hydrogen-enhanced localized plasticity in polycrystalline face-centered cubic metals. *Mech Mater*. 2020;148:103472. <https://doi.org/10.1016/j.mechmat.2020.103472>.
17. Lu X, Zhang X, Shi M, Roters F, Kang G, Raabe D. Dislocation mechanism based size-dependent crystal plasticity modeling

- and simulation of gradient nano-grained copper. *Int J Plasticity*. 2019;113:52–73. <https://doi.org/10.1016/j.iplas.2018.09.007>.
18. Liu J, Ye C, Liu G, Shen Y. Crystal plasticity finite element theoretical models and applications for high temperature, high pressure and high strain-rate dynamic process, Gaoyawli. *Acta High Press Phys*. 2020;34(3):030.
 19. Ling C, Forest S, Besson J, Tanguy B, Latourte F. A reduced micromorphic single crystal plasticity model at finite deformations. Application to strain localization and void growth in ductile metals. *Int J Solids Struct*. 2018;134:43–69. <https://doi.org/10.1016/j.ijsolstr.2017.10.013>.
 20. Vogler TJ, Clayton JD. Heterogeneous deformation and spall of an extruded tungsten alloy: plate impact experiments and crystal plasticity modeling. *J Mech Phys Solids*. 2008;56(2):297–335. <https://doi.org/10.1016/j.jmps.2007.06.013>.
 21. Clayton JD. Modeling dynamic plasticity and spall fracture in high density polycrystalline alloys. *Int J Solids Struct*. 2005;42(16):4613–40. <https://doi.org/10.1016/j.ijsolstr.2005.02.031>.
 22. Wilkerson JW, Ramesh KT. A dynamic void growth model governed by dislocation kinetics. *J Mech Phys Solids*. 2014;70:262–80. <https://doi.org/10.1016/j.jmps.2014.05.018>.
 23. Wilkerson JW, Ramesh KT. A closed-form criterion for dislocation emission in nano-porous materials under arbitrary thermomechanical loading. *J Mech Phys Solids*. 2016;86:94–116. <https://doi.org/10.1016/j.jmps.2015.10.005>.
 24. Clifton R, Raiser G, Ortiz M, Espinosa H, et al. A soft recovery experiment for ceramics. In: Schmidt SC, et al., editors. *Shock compression of condensed matter*. Amsterdam: Elsevier; 1989.
 25. Huang Y. A user-material subroutine incorporating single crystal plasticity in the ABAQUS finite element program. Cambridge: Harvard Univ; 1991.
 26. Czarnota C, Jacques N, Mercier S, Molinari A. Modelling of dynamic ductile fracture and application to the simulation of plate impact tests on tantalum. *J Mech Phys Solids*. 2008;56(4):1624–50.
 27. Meyers MA. *Dynamic behavior of materials*. Hoboken: Wiley; 1994.
 28. Hutchinson JW, Hill R. Bounds and self-consistent estimates for creep of polycrystalline materials. *Proc R Soc Lond A Math Phys Sci*. 1976;348(1652):101–27. <https://doi.org/10.1098/rspa.1976.0027>.
 29. Bassani JL, Wu T-Y. Latent hardening in single crystals. II. Analytical characterization and predictions. *Proc R Soc Lond Ser A Math Phys Sci*. 1893;1991(435):21–41. <https://doi.org/10.1098/rspa.1991.0128>.
 30. Czarnota C, Mercier S, Molinari A. Modelling of nucleation and void growth in dynamic pressure loading, application to spall test on tantalum. *Int J Fract*. 2006;141(1):177–94.
 31. Ledbetter HM, Naimon ER. Elastic properties of metals and alloys. II. Copper. *J Phys Chem Ref Data*. 1974;3(4):897–935. <https://doi.org/10.1063/1.3253150>.
 32. Johnson JN. Dynamic fracture and spallation in ductile solids. *J Appl Phys*. 1981;52(4):2812–25. <https://doi.org/10.1063/1.329011>.

Springer Nature or its licensor holds exclusive rights to this article under a publishing agreement with the author(s) or other rightsholder(s); author self-archiving of the accepted manuscript version of this article is solely governed by the terms of such publishing agreement and applicable law.